Geochemistry Geophysics Geosystems G3

Published by AGU and the Geochemical Society

Article
Volume 13, Number 1
XX Month 2012
QXXXXX, doi:10.1029/2012GC004139
ISSN: 1525-2027

The M7.2 2010 El Mayor-Cucapah earthquake illuminates rheological mantle heterogeneity

Fred F. Pollitz
U.S. Geological Survey, 345 Middlefield Road, MS 977, Menlo Park, California 94025, USA (fpollitz@usgs.gov)

Roland Bürgmann
Department of Earth and Planetary Science, University of California, Berkeley, California 94720, USA

Wayne Thatcher
U.S. Geological Survey, 345 Middlefield Road, MS 977, Menlo Park, California 94025, USA

[1] Major intracontinental strike-slip faults tend to mark boundaries between lithospheric blocks of contrasting mechanical properties along much of their length. Both crustal and mantle heterogeneities can form such boundaries, but the role of crustal versus mantle strength contrasts for localizing strain sufficiently to generate major faults remains unclear. Using the crustal velocity field observed through the Global Positioning System (GPS) in the epicentral area of the M7.2 2010 El Mayor-Cucapah earthquake, Baja California, we find that transient deformation observed after the event is anomalously small in areas of relatively high seismic velocity in the shallow upper mantle ($\sim$50 km depth). This pattern is best explained with a laterally heterogeneous viscoelastic structure that mimics the seismic structure. The mantle of the Southern Colorado River Desert (SCRD) and Peninsular Ranges (PR), which bound the fault system to its east and west, respectively, have anomalously high viscosity and seismic velocity. We hypothesize that compared with the rest of the San Andreas fault (SAF) system to its north, the strike-slip fault system in northern Baja California is narrow because of the presence of the PR and SCRD high-viscosity regions which bound it.

Components: 8100 words, 13 figures.

Keywords: mantle; postseismic; rheology; viscoelasticity.

Index Terms: 1207 Geodesy and Gravity: Transient deformation (6924, 7230, 7240); 1240 Geodesy and Gravity: Satellite geodesy: results (6929, 7215, 7230, 7240); 8162 Tectonophysics: Rheology: mantle (8033).

Received 9 March 2012; **Revised** 24 April 2012; **Accepted** 26 April 2012; **Published** XX Month 2012.

Pollitz, F. F., R. Bürgmann, and W. Thatcher (2012), The M7.2 2010 El Mayor-Cucapah earthquake illuminates rheological mantle heterogeneity, *Geochem. Geophys. Geosyst.*, *13*, QXXXXX, doi:10.1029/2012GC004139.

1. Introduction

[2] *Molnar and Dayem* [2010] examine numerous major strike-slip faults (those with slip rate $\gtrsim$ 10 mm/yr) and document using a wealth of past studies that they tend to be bounded on one side by 'strong' lithosphere. Two issues are whether the existence of such contrasts is a prerequisite for the formation of the faults and whether pre-existing contrasts in the crust versus the mantle are more effective for

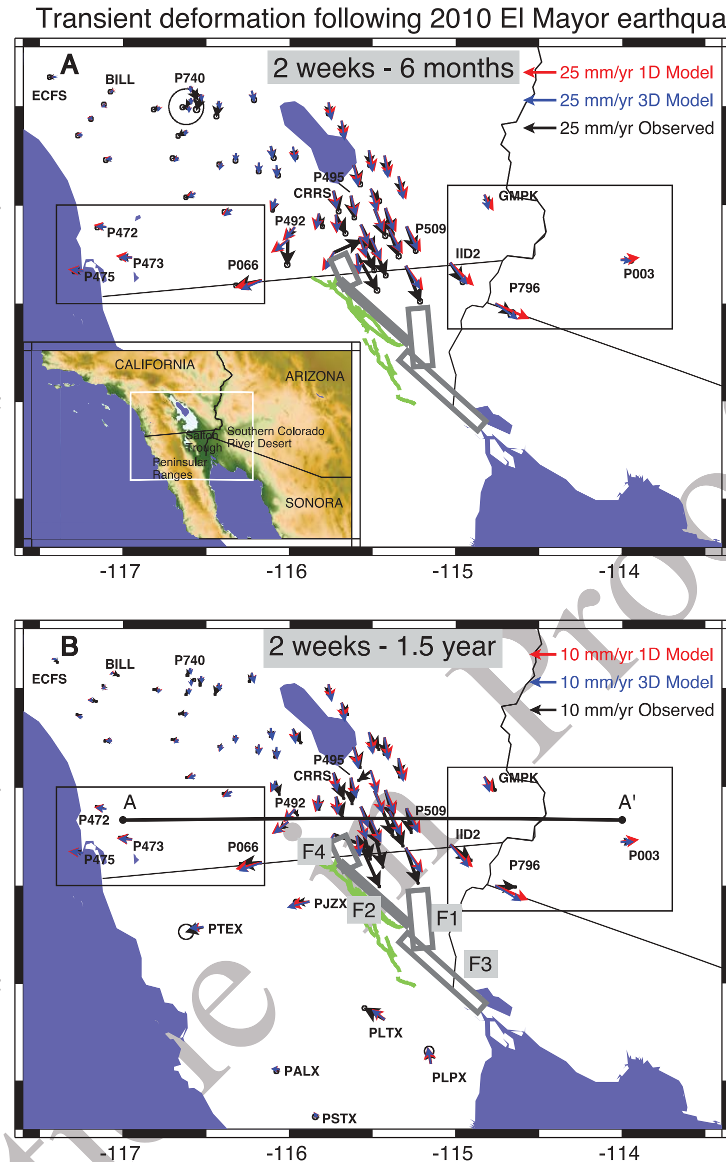

Figure 1. Observed transient deformation following the M7.2 2010 El Mayor-Cucapah earthquake (black vectors) in the time periods (a) 2 weeks to 6 months and (b) 2 weeks to 1.5 years. A model prediction based on the viscoelastic model of *Pollitz* [2003a] and on the 3D viscoelastic model is shown with the red vectors and blue vectors, respectively. (For the later time period, model velocities for PALX, PLPX, PLTX, PTEX, PJZX, and PSTX are for the period 9 months – 1.5 year because of the later start times of these sites.) Fault planes F1, F2, F3, and F4 of *Wei et al.* [2011] are superimposed. In green are the surface traces of the Laguna Salada, Canon Rojo, Cucapah, Pescadores, and Chupamirtos faults. (c and d) Boxed areas of Figure 1a re-plotted in larger scale and (e and f) boxed areas of Figure 1b re-plotted in larger scale.

localizing deformation sufficiently to generate major faults. Although numerical modeling of lithospheric flow is useful for addressing these questions [*Molnar and Dayem*, 2010, and references therein], crustal deformation data can illuminate the mechanical properties of the lithosphere and contribute to the understanding of at least the second issue, i.e. discriminate whether a rheological strength contrast exists in the crust or mantle.

[3] Crustal deformation observed following a large crustal earthquake provides a window into the rheological properties of the crust and underlying mantle. The coseismic stresses imparted by the earthquake relax within the ductile lower crust and mantle, leading to continued deformation of the upper crust. Recordings of these motions by GPS receivers at Earth's surface constrain the mechanical properties of these ductile regions, particularly

 10.1029/2012GC004139

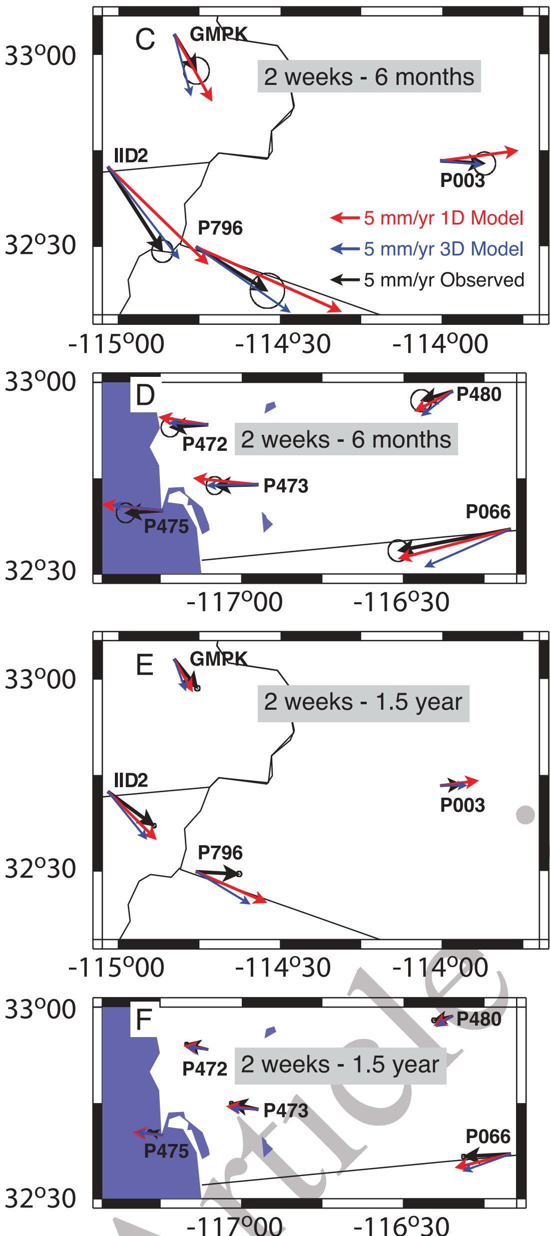

Figure 1. (continued)

viscosity. Results from numerous studies of postseismic relaxation following large continental earthquakes in plate boundary zones yield a picture of a relatively strong lower crust (viscosity $\gtrsim 10^{20}$ Pa s) and relatively weak upper mantle (viscosity $\lesssim 10^{19}$ Pa s), with remaining uncertainty concerning the possible existence of a high-viscosity region in the uppermost ~10 km of the mantle [*Freed et al.*, 2007; *Hammond et al.*, 2009; *Bürgmann and Dresen*, 2008; *Thatcher and Pollitz*, 2008].

[4] The M7.2 April 4, 2010 El Mayor-Cucapah earthquake involved predominantly strike slip along along a ~120-km long set of faults extending from the northern Sierra Cucapah to the Gulf of California [*Wei et al.*, 2011]. The black vectors of Figure 1 show average transient velocity of GPS stations from the continuously operating PBO network, including six new stations installed in response to the earthquake, following the earthquake in two time periods spanning the 1.5 years after the event. These observed horizontal transients, as well as the vertical transients discussed below, have been corrected for background inter-seismic velocities (see section A1) and shallow afterslip and a large M5.7 aftershock (see section A2). We present the interpretation of the postseismic velocity field in terms of viscoelastic relaxation of the surrounding mantle (and to a lesser extent the lower crust), then discuss the implications for the mechanical properties of the surrounding lithosphere.

2. Candidate Models of Postseismic Relaxation

[5] Candidate explanations for the postseismic relaxation are deep afterslip, poroelastic relaxation, and viscoelastic relaxation of the lower crust and upper mantle [*Thatcher*, 1983; *Savage*, 1983; *Savage and Lisowski*, 1998; *Fialko*, 2004; *Freed et al.*, 2007]. The postseismic vertical velocity pattern is an effective discriminant between the deep afterslip and viscoelastic-relaxation models, the former model predicting a quadrant pattern that is positively correlated with the coseismic uplift pattern, and the latter predicting a quadrant pattern – of generally longer wavelength – that is negatively correlated with the coseismic uplift pattern provided that the mantle is of low viscosity relative to the lower crust [*Pollitz et al.*, 2000, 2001; *Freed and Bürgmann*, 2004]. It is also useful for evaluating the poroelastic rebound mechanism, which generally predicts a quadrant pattern of the same sign as the viscoelastic-relaxation mechanism [e.g., *Jónsson et al.*, 2003; *Fialko*, 2004].

2.1. Viscoelastic Relaxation of the Lower Crust and Mantle

[6] For two time periods spanning the first 1.5 years after the El Mayor-Cucapah earthquake, average vertical velocities are evaluated on the laterally homogeneous structure of *Pollitz* [2003a], shown in Figure 2. This model was derived from postseismic relaxation observations following the 1999 Hector Mine, CA earthquake and is characterized by a relatively high-viscosity lower crust and low-viscosity mantle (see section 3.1). Figure 3 compares the

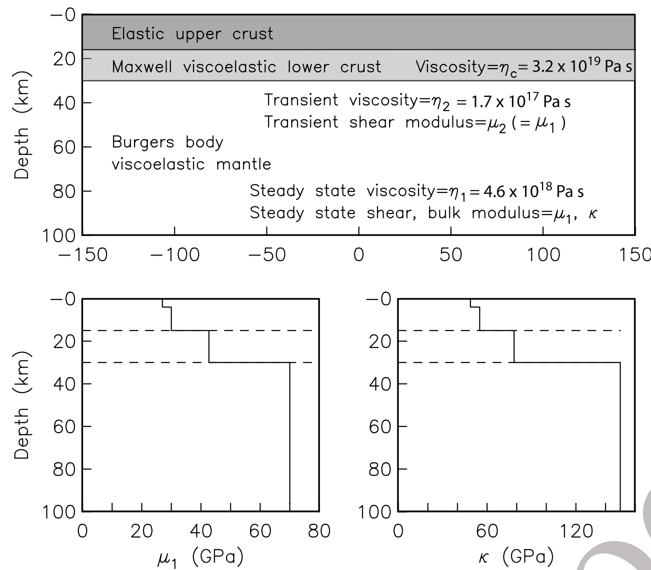

Figure 2. Viscoelastic stratification assumed for the Salton Trough/Cucapah Mtns area, which is the Mojave Desert structure of *Pollitz* [2003a]. Elastic parameters μ_1 and κ are the steady state shear modulus and bulk modulus, respectively. Elastic and viscoelastic parameters are constant in the mantle (depth > 30 km). Note that the mantle is a Jeffreys fluid with transient shear modulus μ_2 equal to the steady state shear modulus μ_1. (Modified from *Pollitz and Thatcher* [2010, Figure 3].)

observed and predicted average velocities. There is a good correlation between quadrants of predicted uplift and observed uplift for both time periods. This comparison is depicted more clearly in Figure 4. The viscoelastic-relaxation model is positively correlated with observed vertical velocities, with correlation coefficients of 0.75 and 0.76 in the considered time periods (Figure 4).

2.2. Deep Afterslip

[7] The deep afterslip model is tested by constructing a model of deep slip beneath the principal strike-slip fault strands (F2 and F3). Uniform slip on these extensions is prescribed over the depth range 15–30 km, and the slip values in the considered time periods are determined by least squares estimation to explain the horizontal postseismic motions. The resulting predicted vertical motions are shown in Figure 5 and compared with observed vertical motions. The negative correlation coefficients in this case (−0.59 and −0.63 in the considered time periods) contrast with the positive correlation coefficients obtained with the viscoelastic-relaxation model and indicate that afterslip alone is not the dominant postseismic process at timescales of one year following the earthquake.

[8] The correlations in the later time period have been determined without two sites – P494 and P506 (Figure 3) – which are outliers in the 2 weeks to 1.5 year period. These two sites lie within the southern Salton Sea geothermal field and may be affected by non-tectonic processes that are not accounted for in our simple methodology to estimate the background velocity field (see section A1). The correlations with the 1D viscoelastic model and afterslip model in this time period are 0.73 and −0.61, respectively, when these sites are included.

2.3. Poroelastic Rebound

[9] A model of combined poroelastic-rebound and afterslip mechanisms was theoretically capable of explaining the joint postseismic horizontal and vertical motions after the 1992 Landers earthquake [*Fialko*, 2004], suggesting it may be applicable to the El Mayor - Cucapah postseismic motions. However, the poroelastic-rebound mechanism may be applicable only over a short time after the event and at relatively short wavelength [*Jónsson et al.*, 2003]. Moreover, the 'combined' mechanism cannot explain the substantial far-field motions observed after the 1999 Hector Mine earthquake [*Freed et al.*, 2007]. We consider poroelastic relaxation of the crust in response to the coseismic stress changes imparted by the El Mayor - Cucapah event. This is calculated as the difference between the static deformation on the *Pollitz* [2003a] elastic structure, which has Poisson's ratio of 0.322 in the upper

Geochemistry Geophysics Geosystems G3
10.1029/2012GC004139

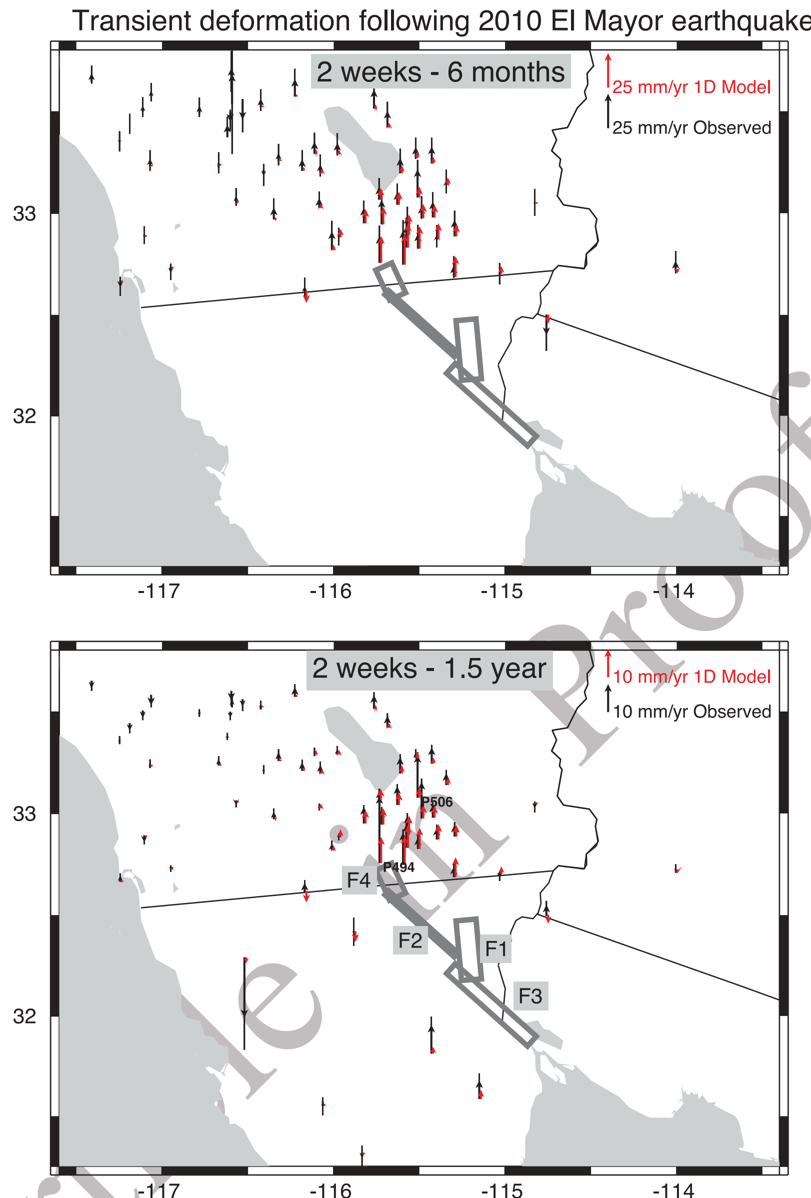

Figure 3. Comparison of average observed and modeled vertical velocities in two postseismic time periods. The modeled velocities are calculated on the *Pollitz* [2003a] viscoelastic structure.

4 km of the crust, and a modified structure where Poisson's ratio is reduced to 0.282 in the upper 4 km. Calculations on these layered elastic structures [*Pollitz*, 1996] yield the net deformation field. The choice of depth range of relaxation is guided by the permeability-depth curve of *Ingebritsen and Manning* [1999], which indicates that permeability in the crust generally decreases rapidly below about 4 km depth. The net relaxation (Figure 6) is dominated by vertical motions that are opposite to the coseismic uplift and concentrated near the source faults. Although these vertical motions are of the correct sign, the restricted spatial scale of both predicted horizontal and vertical postseismic motions is a severe drawback of this mechanism.

3. Lower Crust and Mantle Relaxation

[10] We henceforth consider viscoelastic relaxation of the lower crust and upper mantle to explain observed transient deformation. We implement a two-step approach for evaluating transient crustal deformation following earthquake faulting on a 3D viscosity structure: (1) Define a laterally homogeneous reference structure, and (2) employ perturbation

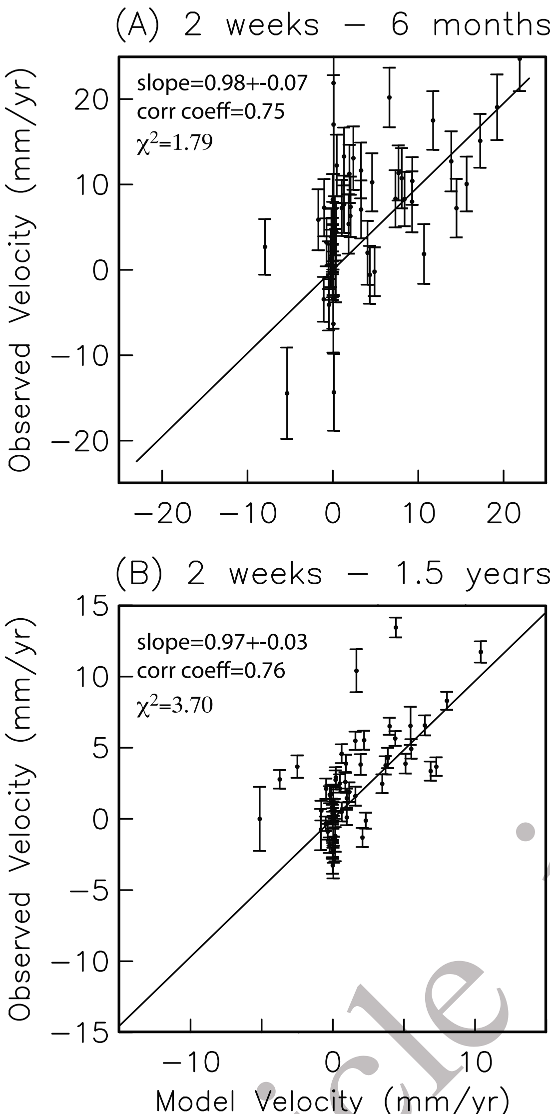

Figure 4. Comparison of average observed and modeled vertical velocities in two postseismic time periods on the 1D reference viscoelastic structure, from Figure 3, converted into ordinate and abscissa values, respectively. Slope of best-fitting line, correlation coefficient, and reduced χ^2 are indicated for each time period. Errors for observed velocities are one-sigma values.

theory to evaluate the deformation on a laterally variable viscosity structure.

3.1. 1D Reference Model

[11] For a laterally homogeneous (i.e. 1D) reference viscoelastic structure, in principle any 1D reference model will suffice, but in practice it is best to choose a reference model that explains a large fraction of the initial variance. For this purpose we consider the laterally homogeneous viscoelastic structure of *Pollitz* [2003a] (Figure 2). This three-layer model prescribes a Maxwell rheology in the lower crust with viscosity $\eta_c = 3.2 \times 10^{19}$ Pa s and transient rheology in the mantle with transient viscosity of $\eta_2 = 1.7 \times 10^{17}$ Pa s and steady state viscosity of $\eta_1 = 4.6 \times 10^{18}$ Pa s. This type of model has been applied successfully to post-earthquake relaxation studies in both continental [*Pollitz*, 2003a, 2005; *Hearn et al.*, 2009] and oceanic [*Panet et al.*, 2010; *Hu*, 2011] settings. To evaluate the suitability of this model as a 1D reference model, we calculate the post-earthquake velocity fields from two variations of it: (1) the same three-layer model with variable η_1, keeping the ratios η_2/η_1 (= 0.037) and η_c/η_1 fixed, and (2) a

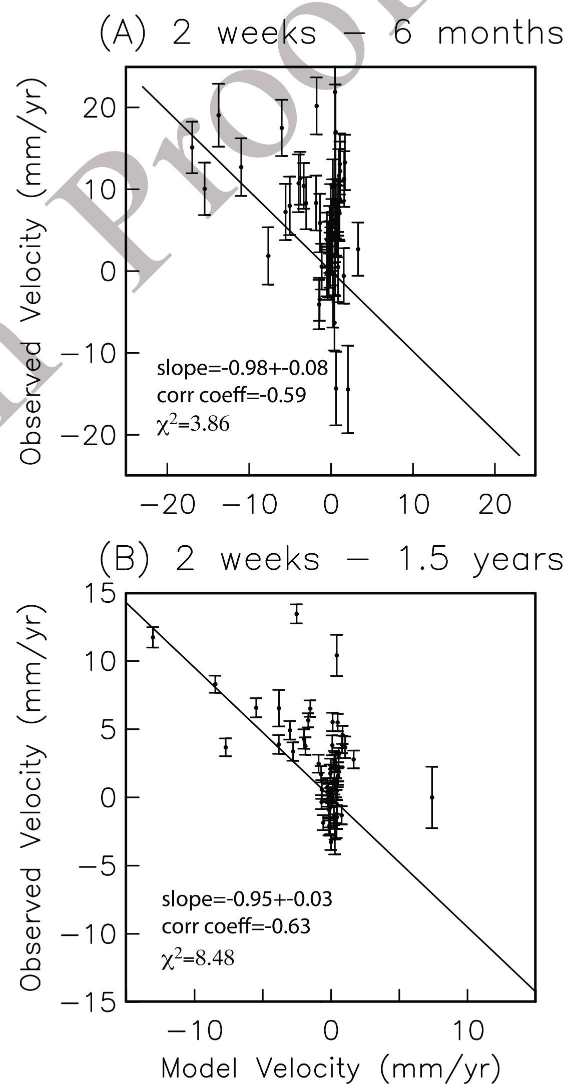

Figure 5. Comparison of average observed and modeled vertical velocities in two postseismic time periods based on the deep afterslip model. Slope of best-fitting line, correlation coefficient, and reduced χ^2 are indicated for each time period. Errors for observed velocities are one-sigma values.

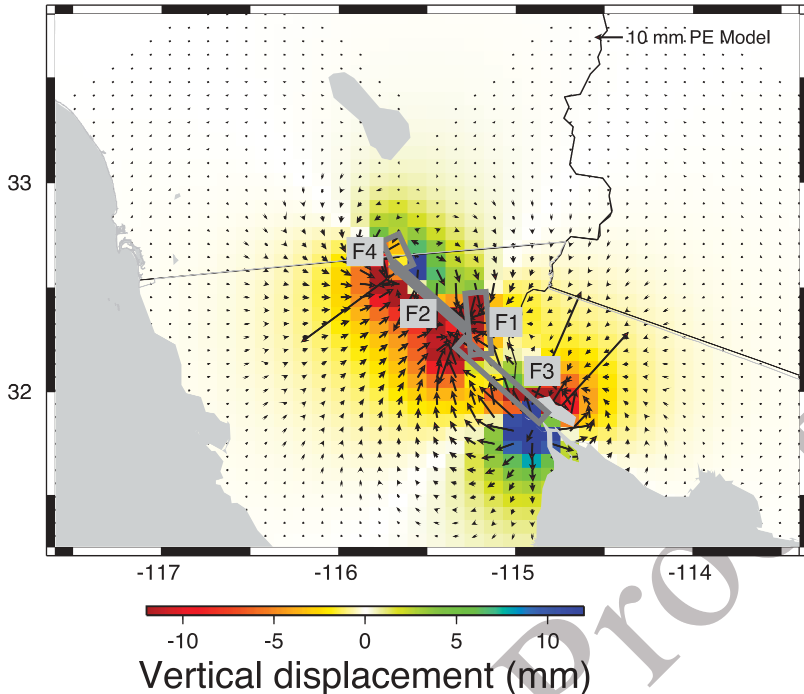

Figure 6. Poroelastic relaxation for the El Mayor - Cucapah event, calculated as the difference between the drained and undrained response with poroelastic flow restricted to the upper 4 km.

four-layer model with an additional layer in the uppermost 10 km of the mantle. We assign this layer a viscosity of $10 \times \eta_1$ based on the proposed existence of a relatively strong layer in the uppermost ~10–20 km of the mantle [*Freed et al.*, 2007]. In this case we again consider variable η_1, keeping η_2/η_1 and η_c/η_1 fixed.

[12] Resulting misfit patterns for these two cases are shown in Figure 7. Results of a variation of these two models with the ratio η_2/η_1 fixed at the value 0.1 are shown in Figure 8. These results indicate that the viscosity structure of *Pollitz* [2003a] has relatively low misfit and is therefore well suited as a 1D reference model. It is consistent with the inference of a relatively high-viscosity lower crust [*Fay and Humphreys*, 2005] and relatively low-viscosity mantle [*Luttrell et al.*, 2007] for the Salton Trough area. Although the range of considered 1D models is not exhaustive, these results also suggest that a thin high-viscosity lid at the top of the mantle is not warranted for this region.

3.2. Methodology on 3D Viscoelastic Structure

[13] Postseismic relaxation on a laterally variable viscosity structure is computed with the method of *Pollitz* [2003b]. This is a semi-analytic method that uses a combination of viscoelastic normal modes to represent the quasi-static displacement field in a truncated spherical harmonic expansion. Starting with the laterally homogenous reference model, the integral equation for the weighting coefficients of these basis functions is solved iteratively, each successive iteration using a more accurate estimate of the quasi-static displacement field in the Laplace transform domain, which then interacts with the laterally heterogeneous viscoelastic structure to update the weighting coefficients. Four iterations are found sufficient to achieve convergence of this solution for each component in the Laplace transform domain, and time domain results are finally obtained through application of an inverse Laplace transform. For all calculations, the earthquake source model of *Wei et al.* [2011] is used to implement the source and calculate postseismic relaxation in specified time periods.

4. Correlation of Transient Velocity With Mantle Seismic Velocity

[14] A model prediction on the (1D) laterally homogeneous viscoelastic structure (section 3.1) with a strong lower crust and low-viscosity upper mantle is shown in Figure 1. Comparison of observed and model velocity fields indicates that observed transient surface velocity is subdued in the SCRD area (e.g. sites P509, IID2, P796, GMPK,

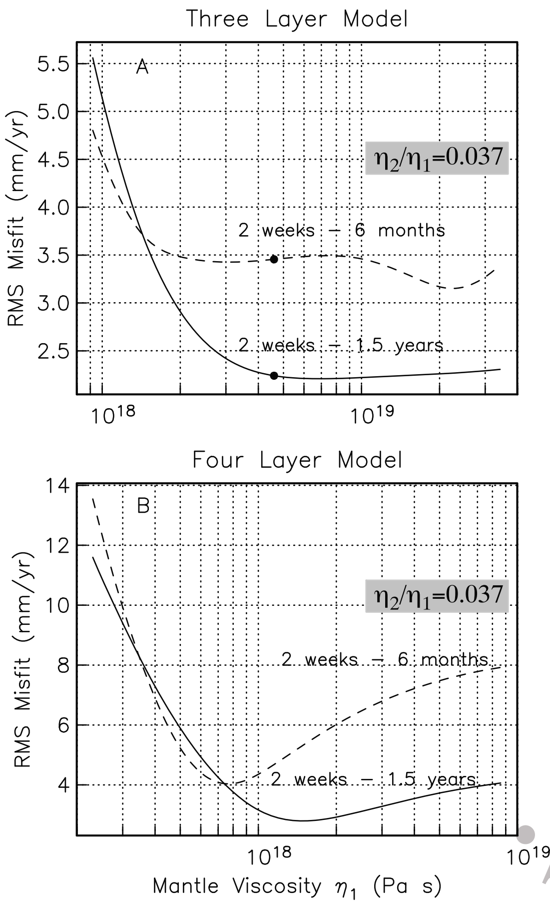

Figure 7. Root-mean square misfit of horizontal velocity in the indicated time periods as a function of steady state mantle viscosity η_1 for (a) three-layer model with uniform-viscosity mantle and (b) four-layer model which includes an additional high-viscosity mantle layer in the uppermost 10 km of the mantle (i.e. from 30 to 40 km depth). Filled circles in Figure 7a correspond to the *Pollitz* [2003a] viscosity model. The ratio of transient to steady state mantle viscosity is η_2/η_1 = 0.037.

and P003) and west toward the PR (e.g. P066, P472, P473, P475, and P480), whereas the observed velocity is elevated in the Salton Trough (ST) area (e.g. CRRS, P495). This is more apparent in Figure A2 (section A3), where East-velocity residuals with respect to the 1D model are systematically positive at western sites and negative at eastern sites. Similarly, transient surface velocities are anomalously large in the southern Salton Sea area, and corresponding North-velocity residuals are systematically negative at sites in this area (Figure A2).

[15] The lower crust and mantle are of relatively high seismic velocity [*Pollitz and Snoke*, 2010], about 2% higher than surrounding regions, in the broad areas of the SCRD and the PR, and they are of anomalously low velocity, about 2% lower than surrounding regions, in the ST (Figure 9). This pattern is corroborated by independent studies [*Yang and Forsyth*, 2006; *Zhang et al.*, 2007; *Yang et al.*, 2008; *Moschetti et al.*, 2010; *Schmandt and Humphreys*, 2010].

[16] A robust measure of the relative amplitude between observed and model horizontal velocity is

$$\text{Relative Amplitude} = \frac{v_{\text{obs}} - v_{\text{model}}}{v_{\text{obs}} + v_{\text{model}}} \tag{1}$$

where v_{obs} and v_{model} are the magnitude of observed and model horizontal velocity vectors, respectively. Using the 1D *Pollitz* [2003a] model as the reference model, a first-order correlation of transient velocity with mantle seismic velocity is apparent in

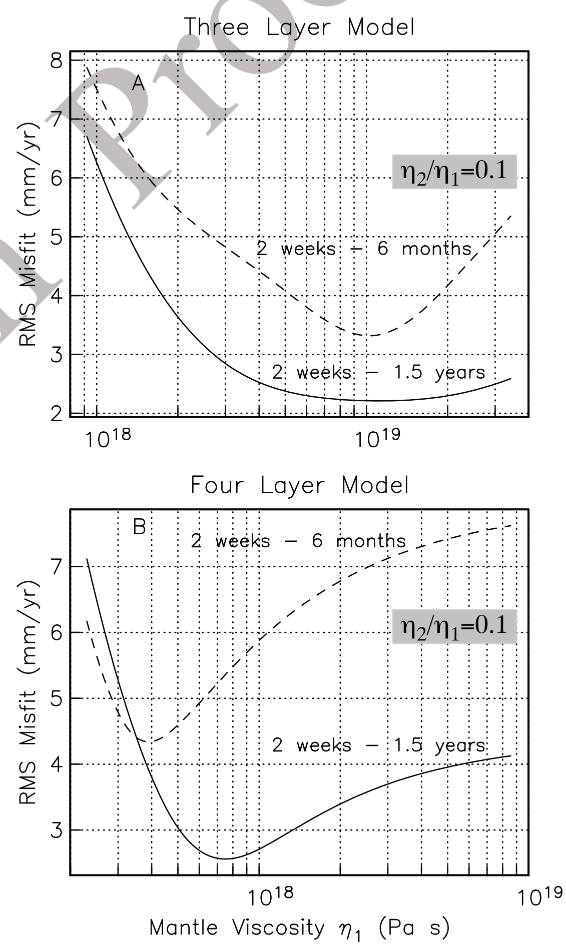

Figure 8. Root-mean square misfit of horizontal velocity in the indicated time periods as a function of steady state mantle viscosity η_1 for (a) three-layer model with uniform-viscosity mantle and (b) four-layer model which includes an additional high-viscosity mantle layer in the uppermost 10 km of the mantle (i.e. from 30 to 40 km depth). The ratio of transient to steady state mantle viscosity is η_2/η_1 = 0.1.

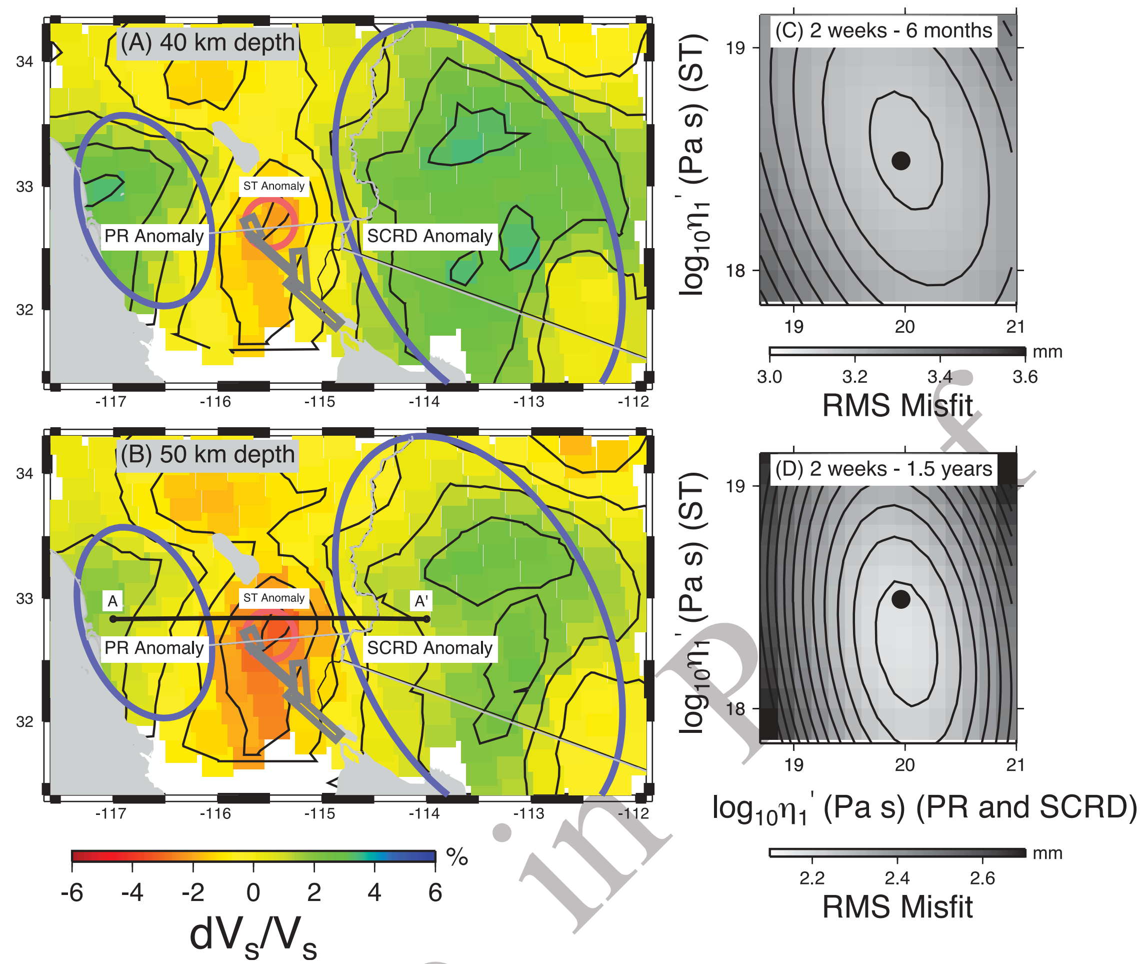

Figure 9. Perturbation in seismic shear wave velocity at (a) 40 km and (b) 50 km depth from surface wave tomography using the dataset and methodology of *Pollitz and Snoke* [2010] with the dataset updated through August, 2011. Contour interval is 1%. Elliptical regions represent three areas (SCRD and PR in blue, ST in red) where the underlying mantle between 30 and 220 km depth is prescribed transient and steady state viscosity values of η_2' and η_1', respectively, their ratio constrained by equation (2). Fault planes F1, F2, F3, and F4 of *Wei et al.* [2011] are superimposed. (c and d) Root-mean square misfit of horizontal velocity in the indicated time periods as a function of η_1' in the ST, PR, and SCRD anomalies; η_1' is assumed identical in the PR and SCRD anomalies. Solid black circle indicates the combination of ST and PR+SCRD anomaly viscosities used in forward models.

Figure 10, which shows the relative amplitude as a function of underlying seismic-shear wave velocity perturbation at 50 km depth (Figure 9b). The large scatter is due, in part, to the preponderance of sites with relatively small transient velocity, which have correspondingly larger errors. Because of the possibility of afterslip not accounted for in our simple model of shallow afterslip (Figure A1), postseismic motion at sites near the northern endpoint of Fault F2 may contain additional signal from unmodeled afterslip. Nevertheless, there is a systematic correlation between relative amplitude and seismic shear wave velocity in both considered time periods, regardless of whether we consider all GPS sites (red lines in Figure 10)) or all sites restricted to be >35 km from the traces of Faults F2 and F3 (black lines), which together accommodated almost all of the coseismic slip. This is confirmed by the negative slopes of the best linear fits to the relative amplitude observations (red and black dashed lines in Figure 10), regardless of the restriction on distance to the fault, which are all consistent with this at >99% confidence.

[17] Based on the general correlation between seismic velocity and mantle viscosity through the intermediary effects of water content and (to a lesser extent) temperature [*Dixon et al.*, 2004], we hypothesize that the reduced transient velocity near the SCRD and PR is caused by relatively high mantle viscosity. Similarly, the elevated transient

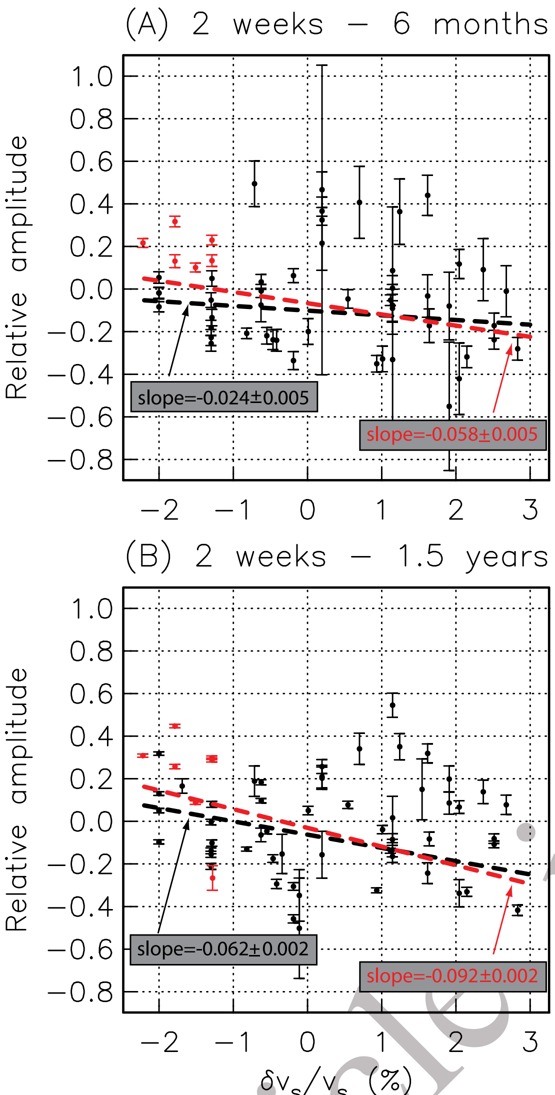

Figure 10. Relative amplitude between observed and model horizontal velocity (defined in equation (1)), plotted with $1-\sigma$ error bars, versus shear wave velocity perturbation $\delta v_s/v_s$ at 50 km depth below each station. Model velocity is that calculated on the 1D model [*Pollitz*, 2003a]. Red and black symbols correspond to all observations less than or greater than 35 km from segments F2/F3, respectively. Dashed red and black lines indicate the best linear fits to all observations (regardless of distance) or observations greater than 35 km from segments F2/F3, respectively; corresponding slope values with $1-\sigma$ errors are indicated.

velocity near the ST is caused by relatively low mantle viscosity.

5. 3D Viscosity Structure

[18] A three-dimensional (3D) model consistent with the seismic data involves two anomalous high-viscosity regions (SCRD and PR) and one low-viscosity region (ST) occupying the elliptical areas shown in Figures 9a and 9b. These are perturbations to the1D reference viscoelastic structure. Within each of the volumes defined over the SCRD, PR, and ST anomalies from 30 to 220 km depth, we test models of anomalous transient viscosity η_2' and steady state viscosity η_1'. To simplify the analysis, we assume that the ratio of the transient to steady state viscosities equals that on the 1D reference model, i.e.

$$\frac{\eta_2'}{\eta_1'} = \frac{\eta_2}{\eta_1} = 0.037 \qquad (2)$$

The lower depth of 220 km marks the nominal base of the asthenosphere, though depth-dependent viscosity structure using postseismic deformation data is generally difficult to resolve deeper than ~60 km depth [*Pollitz and Thatcher*, 2010]. From a grid search over η_1' over the ST and combined PR and SCRD anomalies (Figures 9c and 9d), we find for the SCRD and PR anomalies viscosity values a factor of 20 higher than the 1D model, i.e. $\eta_2' = 3.4 \times 10^{18}$ Pa s and $\eta_1' = 9.2 \times 10^{19}$ Pa s. Within the ST anomaly, we find viscosity values 30% less than the 1D model, i.e. $\eta_2' = 1.2 \times 10^{17}$ Pa s and $\eta_1' = 3.2 \times 10^{18}$ Pa s. Lower viscosity values are not warranted by the GPS data (Figures 9c and 9d).

[19] The horizontal velocity field on this 3D viscoelastic structure is shown by the blue arrows in Figure 1. Figures 1 and A2 show that the 3D model better replicates observed velocities. Following *Freed et al.* [2007], we evaluate quantitative misfit using only far-field sites, defined here as those sites >35 km from the traces of faults F2/F3. Root-mean square (rms) residuals of horizontal velocity (misfit defined as the Euclidean distance between observed and model horizontal velocity vectors) is 3.46 mm/yr and 2.98 mm/yr on the 1D and 3D models, respectively, during the 2 weeks – 6 months period; it is 2.24 mm/yr and 2.15 mm/yr on the 1D and 3D models, respectively, during the 2 weeks – 1.5 years period. An F-test indicates that the reductions in horizontal residuals are significant at the >99.9% and 97.4% confidence levels for the shorter and longer time periods, respectively. The initial RMS (i.e. for a model of no relaxation) is 7.92 mm/yr (2 weeks – 6 months) and 4.39 mm/yr (2 weeks – 1.5 years), so that the 3D model achieves a net variance reduction of 86% and 76% in these time periods, respectively.

6. Discussion

[20] The effect of the viscosity anomalies on the mantle flow is seen in Figure 11, which shows the

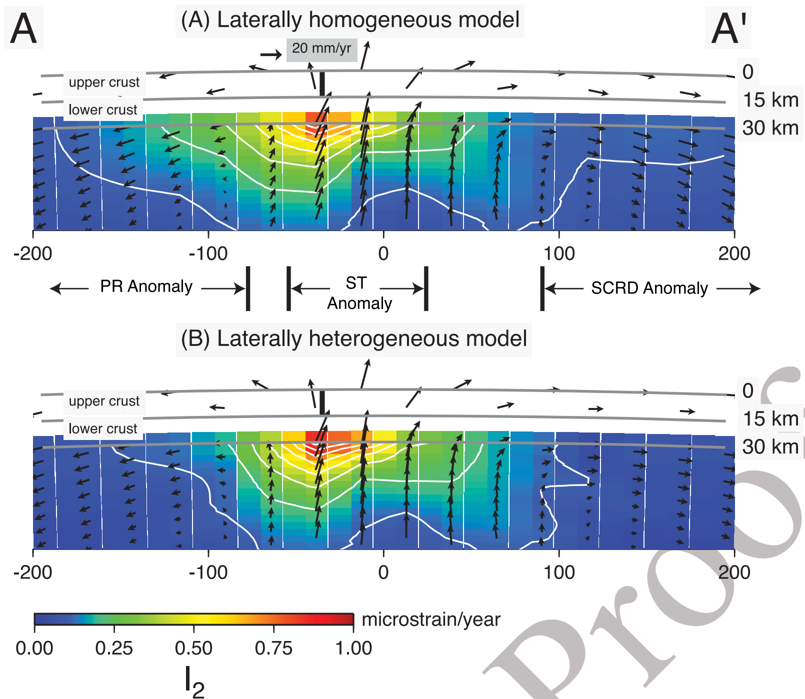

Figure 11. Average velocity for the postseismic period 2 weeks – 6 months on a vertical section along profile AA′ (indicated in Figures 1 and 9) projected onto the profile plane. Superimposed is the second invariant of the strain rate tensor. Thick vertical line indicates the northward projection of the Laguna Salada fault.

average depth-dependent velocity and strain rate fields over the period 2 weeks to 1.5 years. Relative to the 1D model (Figure 11a) the strain rate at depth on the 3D model (Figure 11b) is clearly reduced in the areas of the SCRD and PR high-viscosity anomalies, with a corresponding reduction of horizontal velocity. Similarly, the strain rate at depth is elevated in the area of the low-viscosity ST anomaly.

[21] The existence of contrasts in mechanical properties of the lithosphere is supported by geodetic data [*Hearn et al.*, 2002; *Schmalzle et al.*, 2006; *Özeren and Holt*, 2010; *Ryder et al.*, 2011] and seismic and heat flow data [*Fulton et al.*, 2010; *Molnar and Dayem*, 2010]. A dichotomy of strength contrasts into those of crustal and mantle origin would illuminate the context of how they control associated plate boundary phenomena, e.g. style and type of faulting, the relations between volcanism and faulting, etc., but we do not attempt a thorough examination of this issue here. We may point out that *Fay and Humphreys* [2005] evaluated the effect of elastic heterogeneity arising from the thick Salton Trough sedimentary basin on geodetic velocities; *Malservisi et al.* [2001] used heat flow data to infer upper mantle heterogeneity in the Eastern California Shear Zone; *Fulton et al.* [2010] used interseismic strain accumulation and heat flow data to infer lateral variation in elastic plate thickness as well as Young's modulus across the Carrizo segment of the SAF.

[22] Previous geophysical studies indicate a positive correlation among seismic velocity, low heat flow, and effective elastic plate thickness in the western US [*Humphreys and Dueker*, 1994b; *Lowry et al.*, 2000; *Pollitz et al.*, 2008, 2010], though the correlation may not be as strong globally [*Audet and Bürgmann*, 2011]. *Lowry et al.* [2000] point out a tentative correlation of low heat flow and effective elastic plate thickness, as elevated temperature is expected to reduce the depth of the brittle-ductile transition. The generally low mantle viscosity in the active western US may reflect, to a large extent, the higher heat flow and mantle hydration of the western US relative to the cratonic areas to the east, which emphasizes the dependence of mantle viscosity on the thermal regime and volatile content [*Hyndman et al.*, 2005; *Bürgmann and Dresen*, 2008]. The association of high seismic velocity and high viscosity in the SCRD may highlight the role of volatiles, since heat flow is high throughout the northern Gulf of California and areas eastward [*Blackwell et al.*, 2004]. The area of southeastern California and southwestern Arizona had widespread magmatism

of Laramide age (∼50 MyrBP), thought to be of subduction origin and indicative of relatively thin lithosphere at that time [*Humphreys et al.*, 2003]. Throughout the southern Basin and Range this is overprinted by extension accompanied by magmatism between 25 and 15 MyrBP [*Spencer et al.*, 1995]. *Humphreys* [1995] hypothesizes that pre-existing relatively thin lithosphere was more susceptible to vigorous melting following removal of the Laramide slab and consequent exposure of the lithosphere to ascending asthenosphere. The residual mantle is expected to be dry and depleted of basaltic components and therefore of relatively low density, a hypothesis that is supported by the uppermost mantle density structure given by *Kaban and Mooney* [2001] (their Plate 3). The high seismic velocity arises from the low density; the high viscosity results from the depletion of volatiles. The distribution of 3D mantle viscosity around the northern Gulf of California obtained here supports this scheme of the physical state of the regional mantle. It is consistent with the strong lateral variations in the lithosphere-asthenosphere boundary (LAB) depth [*Lekic et al.*, 2011], supporting the hypothesis that LAB lateral variations reflect lateral variations in rheology [*Lekic et al.*, 2011].

[23] The Peninsular Ranges (PR) batholith is a typical Cordilleran batholith that developed on the edge of the continental margin during the Jurassic to Late Cretaceous [*Silver and Chappell*, 1988; *Todd et al.*, 2003]. As this belt is presently underlain by low-density mantle [*Kaban and Mooney*, 2001], this mantle may represent the depleted and dry residuum from batholith emplacement. A key question is whether the mantle has remained intact since batholith emplacement. Geochemical analyses of rocks exposed by subsequent rapid uplift 80 to 65 MyrBP suggests that the lower crust and mantle roots beneath the northeastern PR may have been removed by flat subduction [*Krummenacher et al.*, 1975; *Grove et al.*, 2003]. The restriction of Laramide-age deformation to the northern PR suggests that Laramide slab descent may have remained deep beneath the southern PR [*Saleeby*, 2003], implying that the mantle beneath the southern PR has remained essentially intact through the Laramide Orogeny.

[24] The existence of relatively strong SCRD and PR mantle may have helped define the locus of tectonism in the Salton Trough and Imperial Valley during the last ∼22 Ma. The record of volcanic and sedimentary rocks indicates that volcanism and associated extension began in the early Miocene [e.g., *Kerr*, 1984]. Incursion of marine sediments in the late Miocene marks the initiation of modern rifting associated with the development of the Gulf of California transtensional system [*Axen and Fletcher*, 1998; *Stock and Hodges*, 1989; *Oskin and Stock*, 2003]. Although rifting since the early Miocene is expected to produce a locally thin lithosphere which is mechanically weaker than its surroundings, the evidence cited above suggests that the SCRD and PR regions have been anomalous for tens of Ma, suggesting that they exerted an influence on the localization of faulting as the rift system in the Gulf of California propagated northward.

7. Conclusions

[25] Our results suggest that the active fault system in northern Baja California occupies a low-viscosity 'trough' in lithospheric strength (i.e. the Salton Trough), bounded on both sides by relatively strong lithosphere (PR and SCRD regions). This is consistent with the defining role of 'strong objects' for concentrating lithospheric strain sufficiently to produce continental faults [*Molnar and Dayem*, 2010]. Our results illustrate that at least in the present case the origin of the strength contrast resides in the mantle. *Molnar and Dayem* [2010] draw a distinction between regions where a clear strength contrast is present, resulting in a dominant fault (e.g. the SAF) and those where it is not, e.g. the Basin and Range. In this context, most of the SAF system in California, broadly defined to include neighboring fault strands, may generally occupy a trough in strength, bounded by the relatively strong Pacific oceanic lithosphere to its west and the Central Valley lithosphere to its east, both of which are known to be of relatively high seismic velocity [e.g., *Humphreys and Dueker*, 1994a; *Moschetti et al.*, 2010]. Thus, major faults appear to occupy plate boundary zones whose width is defined by the high-strength regions which bound it. Where the Central Valley terminates (∼35°N), the SAF system greatly broadens to include the Eastern California Shear Zone [*Dokka and Travis*, 1990], and south of ∼34° the system narrows again because of the presence of the PR and SCRD high-viscosity regions.

Appendix A

A1. Data Analysis

[26] The GPS data product obtained from UNAVCO (http://pboweb.unavco.org/) consists of time series of horizontal displacement with respect to a Stable

 10.1029/2012GC004139

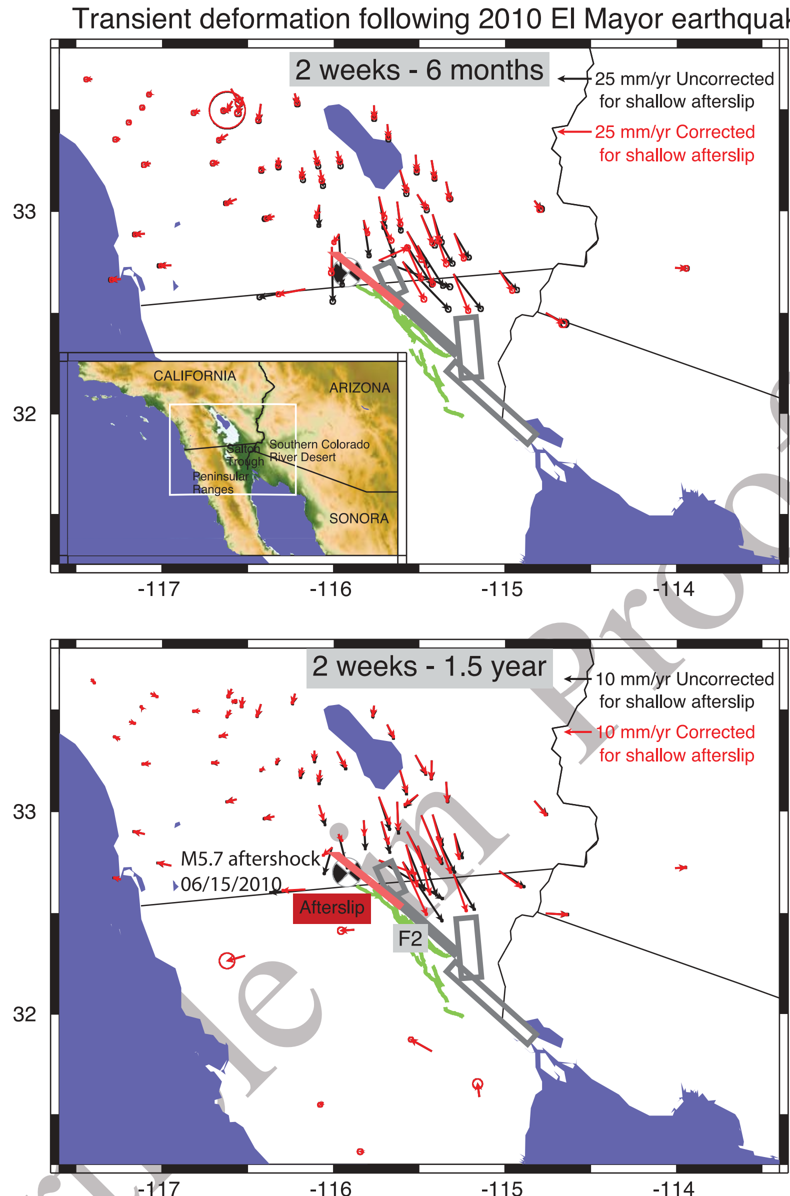

Figure A1. Transient deformation following the M7.2 2010 El Mayor-Cucapah earthquake in two time periods. Black vectors are uncorrected, and red vectors are corrected for shallow afterslip on the fault plane indicated in red, which includes coseismic slip associated with the 06/15/2010 M5.7 aftershock (epicenter and focal mechanism superimposed). Fault planes F1, F2, F3, and F4 of *Wei et al.* [2011] are superimposed; only F2 is labeled. In green are the surface traces of the Laguna Salada, Canon Rojo, Cucapah, Pescadores, and Chupamirtos faults.

North America Reference Frame (SNARF). We have processed this data in three steps:

[27] (1) Pre-earthquake displacement (i.e. at times $t < 2010.259$ – April 4, 2010) is explained with a six-parameter fit using least squares estimation as

$$u_{\mathrm{pre}}(t) = a_1 + a_2 t + a_3 \cos \omega_s t + a_4 \sin \omega_s t + + a_5 \cos \omega_a t + a_6 \sin \omega_a t \qquad \text{(A1)}$$

where $u_{\mathrm{pre}}(t)$ is the pre-earthquake time-dependent displacement of the north or east component, a_1 is a reference displacement, a_2 is the interseismic velocity, a_3 and a_4 are the cosine and sine terms of the semi-annual terms with angular frequency $\omega_s = 2\pi/(0.5 \text{ year})$, and a_5 and a_6 are the cosine and sine terms of the annual terms with angular frequency $\omega_a = 2\pi/(1 \text{ year})$.

10.1029/2012GC004139

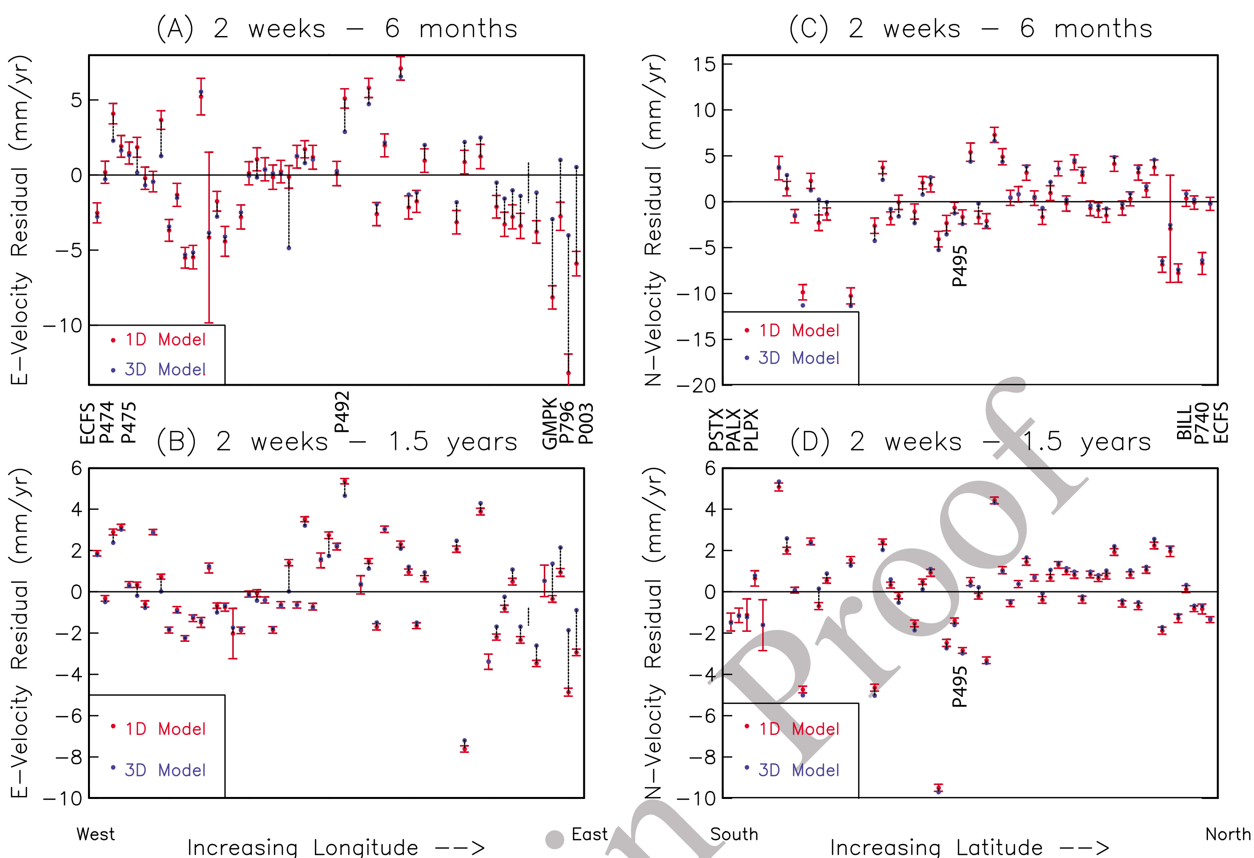

Figure A2. Residual average East-velocity (observed minus modeled) in the (a) 2 weeks to 6 months and (b) 2 weeks to 1.5 year periods, with model crustal velocity calculated on the 1D reference viscoelastic structure (red symbols with error bars) and the 3D model (blue symbols). (c and d) Corresponding results for residual average North-velocity. Sites < 35 km from faults F2/F3 are excluded. Selected sites are labeled (locations in Figure 1 of the main text).

[28] (2) For each of the three Cartesian components, post-earthquake displacement $u(t)$ for $t > 2010.259$ is corrected for interseismic velocity and seasonal terms by subtracting the amount $u_{pre}(t)$ given by equation (A1). Observations at PALX, PLPX, PLTX, PTEX,PJZX, and PSTX began after the earthquake, and for these stations we correct post-seismic horizontal time series for the interseismic velocities determined by *Plattner et al.* [2007] at nearby sites (The Plattner et al. sites INDE, ELCH, SALD, RLOV, LAGH, and MELR for PALX, PLPX, PLTX, PTEX, PJZX, and PSTX, respectively). This is reasonable given the smoothness of the interseismic velocity field in northern Baja California obtained by *Plattner et al.* [2007].

[29] (3) Post-earthquake time series within specific time spans are fit with a best-fitting quadratic function, and corresponding average velocity and velocity error for each component is estimated with least squares estimation assuming a flicker noise model [*Pollitz and Thatcher*, 2010].

A2. Shallow Afterslip Model

[30] Observed horizontal motions around the northern termination of the rupture (black vectors in Figure A1) exhibit systematic misfits which we interpret as the result of afterslip in the months following the El Mayor - Cucapah main shock, including the coseismic slip associated with a M5.7 aftershock on 06/15/2010. We estimated a simple dislocation model to explain the horizontal offsets within ~25 km of the northern termination of fault plane F2. Through a process of trial and error, we obtained the fault length, strike, lower edge depth, northern termination, and amount of right-lateral slip needed to minimize the variance of the observed horizontal velocities in the absence of any viscoelastic relaxation. The upper edge depth (0 km) and dip (90°) were fixed in this procedure, and all slip is assumed to have occurred within the first 6 months following the main shock. The forward problem for static deformation on a layered

spherical structure was solved using the method of *Pollitz* [1996]. We obtained a fault shown by the red trace in Figure A1 with lower edge depth = 8.0 km, length = 45 km, and slip = 17.5 cm. The southern part of the inferred shallow dislocation plane overlaps with the northern portion of fault plane F2 of *Wei et al.* [2011], who found relatively little coseismic slip on the northern ~6 km of plane F2. The northern part covers the rupture area of the M5.7 aftershock. The observed transient velocity fields after correcting for this shallow afterslip are shown by the red vectors in Figure A1. The correction leads to improved fits of our models of transient velocity. Since near-field model predictions are sensitive to the precise details of the shallow afterslip model, which is likely too crude, we restrict our quantitative estimates of misfit to far-field observations (i.e. those sites >35 km from the traces of faults F2 and F3).

A3. Data Residuals

[31] Residual east and north-component velocities with respect to the 1D and 3D viscoelastic models described in the main text are shown in Figure A2. As eastward and northward motions tend to vary as a function of longitude and latitude, respectively, the residuals are plotted as a function of increasing longitude (east component) or latitude (north component). Only far-field sites (>35 km from faults F2 and F3) are included. The residuals in these horizontal components are systematically lower in the 3D model.

Acknowledgments

[32] GPS data of the Plate Boundary Observatory was obtained from the UNAVCO facility. We thank Jim Savage, Jessica Murray-Moraleda, and Andy Freed for their comments on a preliminary draft. This paper benefitted from the comments of Thorsten Becker and ananonymous reviewer.

References

Audet, P., and R. Bürgmann (2011), Global effective elastic thickness, mechanical anisotropy and the supercontinent cycle, *Nat. Geosci.*, *4*, 184–187.

Axen, G. J., and J. M. Fletcher (1998), Late Miocene-Pleistocene extensional faulting, northern Gulf of California, Mexico and Salton Trough, *Int. Geol. Rev.*, *40*, 217–244.

Blackwell, D. D., M. C. Richards, T. Lewis, J. Majorowicz, J. Mareschal, and W. D. E. Gasnold (2004), Geothermal map of North America, scale 1:6,500,000, Am. Assoc. of Pet. Geol., Tulsa, Okla.

Bürgmann, R., and G. Dresen (2008), Rheology of the lower crust and upper mantle: Evidence from rock mechanics, geodesy, and field observations, *Annu. Rev. Earth Planet. Sci.*, *36*, 531–567.

Dixon, J. E., T. H. Dixon, D. R. Bell, and R. Malservisi (2004), Lateral variation in upper mantle viscosity: Role of water, *Earth Planet. Sci. Lett.*, *222*, 451–467.

Dokka, R. K., and C. J. Travis (1990), Role of the eastern California shear zone in accommodating Pacific-North America plate motion, *Geophys. Res. Lett.*, *17*, 1323–1326.

Fay, N. P., and E. D. Humphreys (2005), Fault slip rates, effects of elastic heterogeneity on geodetic data, and the strength of the lower crust in the Salton Trough region, southern California, *J. Geophys. Res.*, *110*, B09401, doi:10.1029/2004JB003548.

Fialko, Y. (2004), Evidence of fluid-filled upper crust from observations of postseismic deformation due to the 1992 M_w7.3 Landers earthquake, *J. Geophys. Res.*, *109*, B08401, doi:10.1029/2004JB002985.

Freed, A. M., and R. Bürgmann (2004), Evidence of powerlaw flow in the Mojave Desert mantle, *Nature*, *430*, 548–551.

Freed, A. M., R. Bürgmann, and T. Herring (2007), Far-reaching transient motions after Mojave earthquakes require broad mantle flow beneath a strong crust, *Geophys. Res. Lett.*, *34*, L19302, doi:10.1029/2007GL030959.

Fulton, P. M., G. Schmalzle, R. N. Harris, and T. Dixon (2010), Reconciling patterns of interseismic strain accumulation with thermal observations across the Carrizo segment of the San Andreas Fault, *Earth Planet. Sci. Lett.*, *300*, 402–406.

Grove, M., O. M. Lovera, and T. M. Harrison (2003), Late Cretaceous cooling of the east-central Peninsular Ranges Batholith (33°N): Relationship to La Posta Pluton emplacement, Laramide shallow subduction, and forearc sedimentation, in *Tectonic Evolution of Northwestern Mexico and the Southwestern USA*, *Spec. Pap. Geol. Soc. Am.*, *374*, 355–379.

Hammond, W. C., C. Kreemer, and G. Blewitt (2009), Geodetic constraints on contemporary deformation in the northern Walker Lane: 3. Central Nevada Seismic Belt postseismic relaxation, in *Late Cenozoic Structure and Evolution of the Great Basin–Sierra Nevada Transition*, *Spec. Pap. Geol. Soc. Am.*, *447*, 33–54.

Hearn, E. H., B. H. Hager, and R. E. Reilinger (2002), Viscoelastic deformation from North Anatolian Fault Zone earthquakes and the eastern Mediterranean GPS velocity field, *Geophys. Res. Lett.*, *29*(11), 1549, doi:10.1029/2002GL014889.

Hearn, E. H., S. McClusky, S. Ergintav, and R. E. Reilinger (2009), Izmit earthquake postseismic deformation and dynamics of the North Anatolian Fault Zone, *J. Geophys. Res.*, *114*, B08405, doi:10.1029/2008JB006026.

Hu, Y. (2011), Deformation processes in great subduction zone earthquake cycles, PhD thesis, Univ. of Victoria, Victoria, B. C., Canada.

Humphreys, E. D. (1995), Post-Laramide removal of the Farallon slab, western United States, *Geology*, *23*, 987–990.

Humphreys, E. D., and K. G. Dueker (1994a), Western U.S. upper mantle structure, *J. Geophys. Res.*, *99*, 9615–9634.

Humphreys, E. D., and K. G. Dueker (1994b), Physical state of the western U.S. upper mantle, *J. Geophys. Res.*, *99*, 9635–9650.

Humphreys, E., E. Hessler, K. Dueker, G. L. Famer, E. Erslev, and T. Atwater (2003), How Laramide-age hydration of North American lithosphere by the Farallon slab controlled subsequent activity in the western United States, *Int. Geol. Rev.*, *45*, 575–595.

Hyndman, R. D., C. A. Currie, and S. P. Mazzotti (2005), Subduction zone backarcs, mobile belts, and orogenic heat, *GSA Today*, *15*, e8–e9, doi:10:1130/1052-5173.

Ingebritsen, S., and C. Manning (1999), Geological implications of a permeability-depth curve for the continental crust, *Geology*, *27*, 1107–1110.

Jónsson, S., P. Segall, R. Pedersen, and G. Björnsson (2003), Post-earthquake ground movements correlated to pore-pressure transients, *Nature*, *424*, 179–183.

Kaban, M. K., and W. D. Mooney (2001), Density structure of the lithosphere in the southwestern United States and its tectonic significance, *J. Geophys. Res.*, *106*, 721–739.

Kerr, D. R. (1984), Early Neogene continental sedimentation in the Vallecito and Fish Creek Mountains, western Salton Trough, California, *Sediment. Geol.*, *38*, 217–246.

Krummenacher, D., R. Gastil, J. Bushee, and J. Dupont (1975), K-Ar apparent ages, Peninsular Ranges batholith, southern California and Baja California, *Geol. Soc. Am. Bull.*, *86*, 760–768.

Lekic, V., S. W. French, and K. M. Fischer (2011), Lithospheric thinning beneath rifted regions of Southern California, *Science*, *334*, 783–787, doi:10.1126/science.1208898.

Lowry, A. R., N. M. Ribe, and R. B. Smith (2000), Dynamic elevation of the Cordillera, western United States, *J. Geophys. Res.*, *105*, 23,371–23,390.

Luttrell, K., D. Sandwell, B. Smith-Konter, B. Bills, and Y. Bock (2007), Modulation of the earthquake cycle at the southern San Andreas fault by lake loading, *J. Geophys. Res.*, *112*, B08411, doi:10.1029/2006JB004752.

Malservisi, R., K. P. Furlong, and T. H. Dixon (2001), Influence of the earthquake cycle and lithospheric rheology on the dynamics of the eastern California shear zone, *Geophys. Res. Lett.*, *28*, 2731–2734.

Molnar, P., and K. E. Dayem (2010), Major intracontinental strike-slip faults and contrasts in lithospheric strength, *Geosphere*, *6*, 444–467.

Moschetti, M. P., M. H. Ritzwoller, F.-C. Lin, and Y. Yang (2010), Crustal shear wave velocity structure of the western United States inferred from ambient seismic noise and earthquake data, *J. Geophys. Res.*, *115*, B10306, doi:10.1029/2010JB007448.

Oskin, M., and J. Stock (2003), Marine incursion synchronous with plate-boundary localization in the Gulf of California, *Geology*, *31*, 23–26.

Özeren, M. S., and W. E. Holt (2010), The dynamics of the eastern Mediterranean and eastern Turkey, *Geophys. J. Int.*, *183*, 1165–1184.

Panet, I., F. Pollitz, V. Mikhailov, M. Diament, P. Banerjee, and K. Grijalva (2010), Upper mantle rheology from GRACE and GPS postseismic deformation after the 2004 Sumatra-Andaman earthquake, *Geochem. Geophys. Geosyst.*, *11*, Q06008, doi:10.1029/2009GC002905.

Plattner, C., R. Malservisi, T. H. Dixon, P. LaFemina, G. F. Sella, J. Fletcher, and F. Suarez-Vidal (2007), New constraints on relative motion between the Pacific Plate and Baja California microplate (Mexico) from GPS measurements, *Geophys. J. Int.*, *170*, 1373–1380.

Pollitz, F. F. (1996), Coseismic deformation from earthquake faulting on a layered spherical Earth, *Geophys. J. Int.*, *125*, 1–14.

Pollitz, F. F. (2003a), Transient rheology of the uppermost mantle beneath the Mojave Desert, California, *Earth Planet. Sci. Lett.*, *215*, 89–104.

Pollitz, F. F. (2003b), Postseismic relaxation theory on a laterally heterogeneous viscoelastic model, *Geophys. J. Int.*, *155*, 57–78.

Pollitz, F. F. (2005), Transient rheology of the upper mantle beneath central Alaska inferred from the crustal velocity field following the 2002 Denali earthquake, *J. Geophys. Res.*, *110*, B08407, doi:10.1029/2005JB003672.

Pollitz, F. F., and J. A. Snoke (2010), Rayleigh-wave phase-velocity maps and three-dimensional shear-velocity structure of the western US from local non-plane surface-wave tomography, *Geophys. J. Int.*, *180*, 1153–1169.

Pollitz, F. F., and W. Thatcher (2010), On the resolution of shallow mantle viscosity structure using postearthquake relaxation data: Application to the 1999 Hector Mine, California, earthquake, *J. Geophys. Res.*, *115*, B10412, doi:10.1029/2010JB007405.

Pollitz, F. F., G. Peltzer, and R. Bürgmann (2000), Mobility of the continental mantle: Evidence from postseismic geodetic observations following the 1992 Landers earthquake, *J. Geophys. Res.*, *105*, 8035–8054.

Pollitz, F. F., C. Wicks, and W. Thatcher (2001), Mantle flow beneath a continental strike-slip fault: Postseismic deformation after the 1999 Hector Mine earthquake, *Science*, *293*, 1814–1818.

Pollitz, F. F., P. McCrory, J. Svarc, and J. R. Murray (2008), Dislocation models of interseismic deformation in the western united states, *J. Geophys. Res.*, *113*, B04413, doi:10.1029/2007JB005174.

Pollitz, F., P. McCrory, D. Wilson, J. Svarc, C. Puskas, and R. Smith (2010), Viscoelastic-cycle model of interseismic deformation in the northwestern United States, *Geophys. J. Int.*, *181*, 665–696.

Ryder, I., R. Bürgmann, and F. F. Pollitz (2011), Lower crustal relaxation beneath the Tibetan Plateau and Qaidam Basin following the 2001 Kokoxili earthquake, *Geophys. J. Int.*, *187*, 613–630, doi:10.1111/j.1365–1246X.2011.05,179.x.

Saleeby, J. (2003), Segmentation of the Laramide Slab—Evidence from the southern Sierra Nevada region, *Geol. Soc. Am. Bull.*, *115*, 655–668.

Savage, J. C. (1983), Strain accumulation in western United States, *Annu. Rev. Earth Planet. Sci.*, *368*, 11–43.

Savage, J. C., and M. Lisowski (1998), Viscoelastic coupling model of the San Andreas fault along the Big Bend, southern California, *J. Geophys. Res.*, *103*, 7281–7292.

Schmalzle, G., T. Dixon, R. Malservisi, and R. Govers (2006), Strain accumulation across the Carrizo segment of the San Andreas Fault, California: Impact of laterally varying crustal properties, *J. Geophys. Res.*, *111*, B05403, doi:10.1029/2005JB003843.

Schmandt, B., and E. Humphreys (2010), Complex subduction and small scale convection revealed by body wave tomography of the western United States upper mantle, *Earth Planet. Sci. Lett.*, *297*, 435–445.

Silver, L. T., and B. W. Chappell (1988), The Peninsular Ranges batholith: An insight into the evolution of the Cordilleran batholiths of southwestern North America, *Trans. R. Soc. Edinburgh Earth Sci.*, *79*, 105–121.

Spencer, J. E., S. M. Richard, S. J. Reynolds, R. J. Miller, M. Shafiqullah, W. G. Gilbert, and M. J. Grubensky (1995), Spatial and temporal relationships between mid-Tertiary magmatism and extension in southwestern Arizona, *J. Geophys. Res.*, *100*, 10,321–10,351.

Stock, J. M., and K. V. Hodges (1989), Pre-Pliocene extension around the Gulf of California and the transfer of Baja California to the Pacific plate, *Tectonics*, *8*, 99–115.

Thatcher, W. (1983), Nonlinear strain buildup and the earthquake cycle on the San Andreas fault, *J. Geophys. Res.*, *88*, 5893–5902.

Thatcher, W., and F. F. Pollitz (2008), Temporal evolution of continental lithospheric strength in actively deforming regions, *GSA Today*, *18*, 4–11.

Todd, V. R., S. E. Shaw, and J. M. Hammarstrom (2003), Cretaceous plutons of the Peninsular Ranges Batholith, San Diego and westernmost Imperial Counties, California: Intrusion across a Late Jurassic continental margin, in *Tectonic Evolutionof Northwestern Mexico and the Southwestern USA*, *Spec. Pap. Geol. Soc. Am.*, *374*, 185–235.

Wei, S., et al. (2011), Superficial simplicity of the 2010 El Mayor-Cucapah earthquake of Baja California in Mexico, *Nat. Geosci.*, *4*, 615–618, doi:10.1038/ngeo1213.

Yang, Y., and D. W. Forsyth (2006), Rayleigh wave phase velocities, small-scale convection, and azimuthal anisotropy beneath southern California, *J. Geophys. Res.*, *111*, B07306, doi:10.1029/2005JB004180.

Yang, Y., M. H. Ritzwoller, F. C. Lin, M. P. Moschetti, and N. M. Shapiro (2008), Structure of the crust and uppermost mantle beneath the western United States revealed by ambient noise and earthquake tomography, *J. Geophys. Res.*, *113*, B12310, doi:10.1029/2008JB005833.

Zhang, X., H. Paulssen, S. Lebedev, and T. Meier (2007), Surface wave tomography of the Gulf of California, *Geophys. Res. Lett.*, *34*, L15305, doi:10.1029/2007GL030631.